A comparative analysis of Lagrange multiplier and penalty approaches for modelling fluid-structure interaction

Brandsen, Jacobus D.; Viré, Axelle; Turteltaub, Sergio R.; Van Bussel, Gerard J.W.

DOI
10.1108/EC-04-2020-0183

Publication date
2020

Document Version
Final published version

Published in
Engineering Computations (Swansea, Wales)

Citation (APA)
Brandsen, J. D., Viré, A., Turteltaub, S. R., & Van Bussel, G. J. W. (2020). A comparative analysis of Lagrange multiplier and penalty approaches for modelling fluid-structure interaction. *Engineering Computations (Swansea, Wales)*, *38*(4), 1677-1705. https://doi.org/10.1108/EC-04-2020-0183

A comparative analysis of Lagrange multiplier and penalty approaches for modelling fluid-structure interaction

Jacobus D. Brandsen
Wind Energy Group, and Aerospace Structures and Computational Mechanics Group, Faculty of Aerospace Engineering, Delft University of Technology, Delft, The Netherlands

Axelle Viré
Wind Energy Group, Faculty of Aerospace Engineering, Delft University of Technology, Delft, The Netherlands

Sergio R. Turteltaub
Aerospace Structures and Computational Mechanics Group, Faculty of Aerospace Engineering, Delft University of Technology, Delft, The Netherlands, and

Gerard J.W. Van Bussel
Wind Energy Group, Faculty of Aerospace Engineering, Delft University of Technology, Delft, The Netherlands

Received 1 April 2020
Revised 29 June 2020
23 July 2020
Accepted 4 August 2020

Abstract

Purpose – When simulating fluid-structure interaction (FSI), it is often essential that the no-slip condition is accurately enforced at the wetted boundary of the structure. This paper aims to evaluate the relative strengths and limitations of the penalty and Lagrange multiplier methods, within the context of modelling FSI, through a comparative analysis.

Design/methodology/approach – In the immersed boundary method, the no-slip condition is typically imposed by augmenting the governing equations of the fluid with an artificial body force. The relative accuracy and computational time of the penalty and Lagrange multiplier formulations of this body force are evaluated by using each to solve three test problems, namely, flow through a channel, the harmonic motion of a cylinder through a stationary fluid and the vortex-induced vibration (VIV) of a cylinder.

Findings – The Lagrange multiplier formulation provided an accurate solution, especially when enforcing the no-slip condition, and was robust as it did not require “tuning” of problem specific parameters. However, these benefits came at a higher computational cost relative to the penalty formulation. The penalty formulation achieved similar levels of accuracy to the Lagrange multiplier formulation, but only if the appropriate penalty factor was selected, which was difficult to determine a priori.

Originality/value – Both the Lagrange multiplier and penalty formulations of the immersed boundary method are prominent in the literature. A systematic quantitative comparison of these two methods is

---

This work was supported by the Rijksdienst voor Ondernemend Nederland (RVO) under the TSE Hernieuwbare Energie funding scheme (ABIBA project).

Engineering Computations
© Emerald Publishing Limited
0264-4401
DOI 10.1108/EC-04-2020-0183

presented within the same computational environment. A novel application of the Lagrange multiplier method to the modelling of VIV is also provided.

Keywords Penalty, Finite element, Fluid-structure interaction, Lagrange multiplier, Immersed boundary

Paper type Research paper

1. Introduction

Structures that operate under conditions in which their dynamics are strongly coupled to that of the surrounding fluid are pervasive in engineering. Examples of such fluid-structure interaction (FSI) include the aeroelastic deformations of propellers (Sodja *et al.*, 2018), the wave-induced motions of floating wind turbines (Yan *et al.*, 2016) and floods caused by dam-breaks (Amicarelli *et al.*, 2017). For design purposes, numerical simulations are an attractive option as a large number of different geometries, configurations and load cases can easily be considered, while minimising expensive laboratory and field testing. A popular approach to simulating FSI is to adopt a partitioned scheme, wherein the fluid and structural dynamics are each calculated separately using two different solvers. The interaction between fluid and structure is accounted for by letting the solvers exchange information about the deformation of the wetted boundary of the structure and the traction exerted on this boundary by the fluid.

The approaches for achieving a partitioned scheme can be divided into two different groups. In the first group, which have been referred to as defined-body (DB) methods (Viré *et al.*, 2015) or body-conformal grid methods (Mittal and Iaccarino, 2005), the domain of the fluid dynamics model conforms to the shape of the wetted boundary of the structure. The wetted boundary is, therefore, an external boundary of the domain in the fluid dynamics model and the structure is located entirely outside of this domain. The no-slip condition that exists at the wetted boundary is imposed in the fluid dynamics model through Dirichlet boundary conditions. DB methods have been used to investigate FSI in a wide variety of applications such as the vibration of wind turbines (Bazilevs *et al.*, 2011) and axial compressor rotors (Brandsen *et al.*, 2018), the deployment of spacecraft parachutes (Gao *et al.*, 2016) and the response of submersible hulls to underwater explosions (Gong, 2019). The second group, called immersed boundary methods, are the focus of this article. In an immersed boundary method, the shape of the domain of the fluid dynamics model does not conform to that of the structure. Instead, it contains both the space occupied by the structure and the space occupied by the fluid. Therefore, the wetted boundary is located entirely within the domain and no longer constitutes an external boundary. Typically, the no-slip condition at the wetted boundary is indirectly enforced by adding an artificial body force term to the governing equations of the fluid. The artificial body force causes the velocity of the fluid to approach that of the structure at this boundary.

The origin of immersed boundary methods can be traced back to the method of Peskin (1972), who used it to simulate the motion of heart valve leaflets. Since then, the immersed boundary method has been developed further by authors such as Taira and Colonius (2007), who combined it with a predictor-corrector time integration scheme and Lācis *et al.* (2016), who adapted it to particulate flows. The fictitious domain method, a variant of the immersed boundary method, has also since been developed for simulating FSI. Two common approaches that are actively being investigated in the literature are to use either a Lagrange multiplier or a penalty formulation for the artificial body force. An example of a specific Lagrange multiplier approach that is currently popular is the distributed Lagrange multiplier (DLM) method. Authors who have applied the DLM method within the immersed boundary or fictitious domain methods include Glowinski *et al.* (1995), Glowinski *et al.* (1997, 1998), Boffi *et al.* (2015), Boffi and Gastaldi (2017), Kadapa *et al.* (2016) and Sun (2019). Examples of the penalty approach being used within the immersed boundary or fictitious domain methods are Goldstein *et al.* (1993), Khadra *et al.* (2000), Viré *et al.* (2012, 2015), Viré *et al.* (2016), Kim and Peskin (2016), Verma *et al.* (2017) and Specklin and Delauré (2018).

The purpose of this article is to conduct a systematic and quantitative comparative analysis of the two popular methods of enforcing the no-slip condition for FSI within the context of the immersed boundary or fictious domain methods, namely, the penalty and Lagrange multiplier. To highlight the effects of the different formulations of these approaches, test problems with relatively simple fluid and structural dynamics are selected for the analysis. This increases the likelihood that any disparities in performance observed between the approaches are not caused by difficulties in modelling the physics of the test problems, but are instead the result of the formulations used. The test problems were, therefore, limited to ones involving laminar flow past stationary or moving rigid structures. The article begins by presenting the continuous formulation of both approaches in Section 2. The spatial and temporal discretisations are covered in Sections 3 and 4, respectively. Section 5 presents the results of the comparative analysis using a number of test problems. Finally, conclusions and recommendations are provided in Section 6.

2. Continuous formulation

2.1 Governing equations of the fluid

Consider the domain Ω of the FSI problem that is illustrated in Figure 1, which is set in a d-dimensional space. The domain contains a moving solid body, $\Omega_s = \Omega_s(t)$, surrounded by an incompressible Newtonian fluid, $\Omega_f = \Omega_f(t)$ so that the overall domain is $\Omega = \Omega_s \cup \Omega_f$. Note that in this case, Ω is not a function of time t. The boundaries of Ω_s and Ω are denoted by $\partial\Omega_s$ and $\partial\Omega$, respectively. In the immersed boundary and fictitious domain methods, the governing equations of the fluid are solved throughout the entire domain Ω, with Ω_s being treated as though it is filled with the same fluid as Ω_f. The domain boundary $\partial\Omega = \partial\Omega_D \cup \partial\Omega_N$ is divided such that $\partial\Omega_D$ denotes the portion of the boundary on which Dirichlet boundary

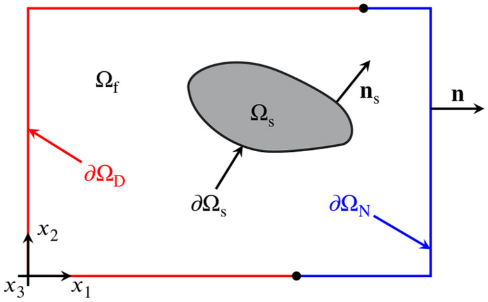

Notes: The external boundary of the domain is given by $\partial\Omega = \partial\Omega_D \cup \partial\Omega_N$, where $\partial\Omega_D$ and $\partial\Omega_N$ are the portions of the boundary on which the Dirichlet boundary conditions for the fluid velocity and the traction (Neumann) boundary conditions are prescribed, respectively. The wetted boundary of the structure is $\partial\Omega_s$. The unit vectors $\mathbf{n}$ and $\mathbf{n}_s$ are normal to $\partial\Omega$ and $\partial\Omega_s$, respectively

Figure 1. Domain $\Omega = \Omega_s \cup \Omega_f$ of a generic fluid-structure interaction problem, consisting of a solid body Ω_s surrounded by an incompressible Newtonian fluid Ω_f

conditions are specified for the velocity field of the fluid, and $\partial\Omega_N$ is the complementary portion on which tractions are applied (Neumann boundary conditions). The unit vector $\mathbf{n}$ is normal to $\partial\Omega$ and points out of Ω. Similarly, the unit vector $\mathbf{n}_s$ is normal to $\partial\Omega_s$ and points out of $\Omega_{s.}$

If the body is rigid, the governing equations of the fluid can be formulated as:

$$\rho\frac{\partial\mathbf{u}}{\partial t}+\rho(\nabla\mathbf{u})\mathbf{u}=\nabla\boldsymbol{\sigma}+\mathbf{b}+\mathbf{f}_{\mathrm{s}},\quad \text{in }\ \Omega\times(0,t] \tag{1a}$$

$$\boldsymbol{\sigma}=-\mathrm{p}\mathbf{I}+\mu\left(\nabla\mathbf{u}+(\nabla\mathbf{u})^{\mathrm{T}}\right),\qquad \text{in }\ \Omega\times(0,\mathrm{t}] \tag{1b}$$

$$\operatorname{div}\ \mathbf{u}=0,\qquad \text{in }\ \Omega\times(0,t] \tag{1c}$$

$$\mathbf{u}_{\mathrm{s}}(\mathbf{x},t)=\overline{\mathbf{u}}(t)+\overline{\boldsymbol{\omega}}(t)\times(\mathbf{x}-\overline{\mathbf{x}}(t)),\quad \text{in }\ \Omega_{\mathrm{s}}\times(0,t] \tag{1d}$$

$$\mathbf{u}(\mathbf{x},t)=\hat{\mathbf{u}}(\mathbf{x},t),\quad \text{on }\ \partial\Omega_{\mathrm{D}}\times(0,t] \tag{1e}$$

$$\boldsymbol{\sigma}(\mathbf{x},\mathrm{t})\mathbf{n}(\mathbf{x},\mathrm{t})=\hat{\mathbf{t}}(\mathbf{x},\mathrm{t}),\quad \text{on }\ \partial\Omega_{\mathrm{N}}\times(0,\mathrm{t}] \tag{1f}$$

$$\mathbf{u}(\mathbf{x},0)=\mathbf{u}_0(\mathbf{x}),\quad \text{in }\ \Omega \tag{1g}$$

$$p(\mathbf{x},0)=p_0(\mathbf{x}),\quad \text{in }\ \Omega \tag{1h}$$

$$\mathbf{f}_{\mathrm{s}}=\mathbf{f}_{\mathrm{s}}(\mathbf{x},t)\quad \text{such that}\quad \mathbf{u}=\mathbf{u}_{\mathrm{s}},\text{in }\ \Omega_{\mathrm{s}}\times(0,t] \tag{1i}$$

where $\mathbf{x}$ signifies the coordinates of a point in Ω, ρ is the density of the fluid, μ is its dynamic viscosity, p is its pressure, $\mathbf{u}$ is its velocity, $\boldsymbol{\sigma}$ is the Cauchy stress tensor, $\mathbf{I}$ is the identity tensor and $\mathbf{b}$ is a gravity-like body force. The boundary conditions specified for $\mathbf{u}$ and the traction are denoted, respectively, by $\hat{\mathbf{u}}$ and $\hat{\mathbf{t}}$. The initial condition assigned to $\mathbf{u}$ is represented by $\mathbf{u}_0$. Similarly, the initial condition assigned to p is signified by p_0. The vectors $\overline{\mathbf{x}}$ and $\overline{\mathbf{u}}$ denote the coordinates and velocity, respectively, of the centre of gravity of the solid body and $\overline{\boldsymbol{\omega}}$ is the body's angular velocity. The resulting velocity field of the body is represented by $\mathbf{u}_s$. The term $\mathbf{f}_s$ is an artificial body force that imposes the no-slip condition by ensuring that $\mathbf{u} = \mathbf{u}_s$ in $\Omega_{s.}$

Equation (1a) is the balance of linear momentum of the fluid and its weak form is given by:

$$\begin{aligned}\int_{\Omega}\mathbf{w}\cdot\rho\frac{\partial\mathbf{u}}{\partial t}\ d\Omega=\rho\int_{\Omega}\mathbf{u}\cdot(\nabla\mathbf{w})\mathbf{u}\ d\Omega-\rho\int_{\partial\Omega}(\mathbf{u}\cdot\mathbf{w})(\mathbf{u}\cdot\mathbf{n})\ dS\\ -\int_{\Omega}\mathbf{w}\cdot\nabla p\ d\Omega-\mu\int_{\Omega}\nabla\mathbf{w}\cdot\nabla\mathbf{u}\ d\Omega\\ +\mu\int_{\partial\Omega}(\nabla\mathbf{u})^{T}\mathbf{w}\cdot\mathbf{n}\ dS+\int_{\Omega}\mathbf{w}\cdot\mathbf{b}\ d\Omega\\ +\int_{\Omega}\mathbf{w}\cdot\mathbf{f}_{\mathrm{s}}\ d\Omega,\end{aligned} \tag{2}$$

which is satisfied for all test functions **w**. The functional space of **w** is the same as that of **u**, with the exception that **w** vanishes on the portion of $\partial\Omega_D$ on which strong Dirichlet boundary conditions for **u** are specified. Similarly, the weak form of the continuity equation (equation (1c)) is:

$$\int_\Omega q \ \operatorname{div}\mathbf{u} \ d\Omega = 0, \tag{3}$$

which is satisfied for all test functions q that are from the same functional space as p.

2.2 Penalty approach

The immersed body (IB) method (Viré *et al.*, 2016), from the open-source numerical tool *Fluidity*, is selected to represent the penalty approach in the comparative analysis. *Fluidity* is a finite-element (FE) code that is capable of solving the Navier–Stokes equations on structured and unstructured meshes (Pain *et al.*, 2005; Pain *et al.*, 2001; Piggott *et al.*, 2008). In the IB method, the artificial body force term has the form:

$$\mathbf{f}_\mathrm{s} = \beta\,\alpha_\mathrm{s}(\mathbf{u}_\mathrm{s} - \mathbf{u}), \tag{4}$$

where β is a constant penalty factor and α_s is the solid concentration field. The latter tracks the volume fraction of solid material at each point in Ω at time t and is defined by:

$$\alpha_\mathrm{s}(\mathbf{x}, t) = \begin{cases} 1 & \text{if } \mathbf{x} \in \Omega_\mathrm{s}(t), \\ 0 & \text{if } \mathbf{x} \notin \Omega_\mathrm{s}(t). \end{cases} \tag{5}$$

To satisfy the no-slip condition, the velocity of the fluid must be equal to the velocity of the structure throughout Ω_s. This is achieved by selecting β to be large enough to allow $\mathbf{f}_\mathrm{s}$ to become the dominant term in equation (1a) for $\mathbf{x} \in \Omega_\mathrm{s}(t)$, hence forcing the difference between $\mathbf{u}_\mathrm{s}$ and **u** to be small in this region. An advantage of the penalty approach is that it is simple and does not require any modifications to the governing equations of the fluid, apart from the inclusion of the artificial body force. However, a limitation is that the difference between $\mathbf{u}_s$ and **u** can never be exactly zero as this would result in $\mathbf{f}_\mathrm{s}$ also becoming zero. The penalty approach is, therefore, incapable of imposing the no-slip condition exactly. Nonetheless, this limitation is acceptable as long as the difference between $\mathbf{u}_s$ and **u** is small enough to accurately account for the influence of the body on the surrounding fluid.

2.3 Distributed Lagrange multiplier approach

In the DLM method, the artificial body force is set equal to:

$$\mathbf{f}_\mathrm{s} = \alpha_\mathrm{s}\boldsymbol{\lambda}, \tag{6}$$

where λ is a Lagrange multiplier field whose vector components are functions in $L^2(\Omega_\mathrm{s})$. A weak version of the no-slip condition is also introduced:

$$\int_{\Omega_\mathrm{s}} \boldsymbol{\gamma}\cdot(\mathbf{u}_\mathrm{s} - \mathbf{u}) \ d\Omega = 0, \tag{7}$$

which is satisfied for all test functions $\boldsymbol{\gamma}$ from the same functional space as $\boldsymbol{\lambda}$. The latter has to be solved for during the time integration of the governing equations, together with the fields **u** and p, while satisfying equation (7).

Note that $\mathbf{f}_s$ does not contain the quantity ($\mathbf{u}_s - \mathbf{u}$). Consequently, this quantity is allowed to be equal to zero for $\mathbf{x} \in \Omega_s(t)$, while still ensuring a non-zero value for $\mathbf{f}_s$. Therefore, unlike the penalty approach, the DLM approach is theoretically capable of enforcing the no-slip condition exactly. However, this advantage comes at the cost of introducing an additional solution variable and constraint equation.

2.4 Governing equations of the structure

The comparative analysis considers both one-way FSI test problems, in which the motion of the structure is prescribed and two-way FSI test problems, where the structure responds dynamically to the traction exerted on it by the fluid. For the two-way FSI problems, the structure will be modelled as a rigid body of mass m attached to a linear spring, with spring constant k and a viscous damper, with damping coefficient c. The spring and damper represent the stiffness and internal damping, respectively, that would be possessed by a flexible structure. Furthermore, the motion of the rigid body is constrained so that it cannot rotate and can only translate in the x_1-direction. The response of the body, therefore obeys the equation of motion of a single-degree-of-freedom oscillator:

$$m\bar{a}_1 + c\bar{u}_1 + k\bar{x}_1 = \bar{t}_1. \tag{8}$$

The subscript in equation (8) denotes the vector components of $\bar{\mathbf{a}}$, $\bar{\mathbf{u}}$, $\bar{\mathbf{x}}$ and $\bar{\mathbf{t}}$, acting in the x_1-direction, where $\bar{\mathbf{a}} = d\bar{\mathbf{u}}/dt$ is the linear acceleration at the centre of gravity of the structure. The quantity $\bar{\mathbf{t}}$ is the resultant traction exerted on the structure by the fluid:

$$\bar{\mathbf{t}} = \int_{\partial\Omega_s} \boldsymbol{\sigma}(\mathbf{x}, \mathrm{t})\mathbf{n}_s(\mathbf{x}, t) \; dS. \tag{9}$$

3. Spatial discretisation

In this section, the spatially discretised governing equations are discussed. Firstly, the spatially discretised equations that are common to both the penalty and the Lagrange multiplier approaches are presented. This is followed by the discretisation of the artificial body force for each approach. Finally, the influence of this discretisation on the calculation of the traction exerted on the structure by the fluid is addressed.

3.1 Governing equations of the fluid

A mesh of finite elements is created from Ω. The union of these elements form a new domain Ω^h such that $\Omega^h \approx \Omega$. Discontinuous piece-wise linear shape functions ($\mathrm{P1}_{\mathrm{DG})}$ are chosen to represent $\mathbf{u}$ and continuous quadratic polynomials (P2) are selected to represent p. An advantage of this combination of discretisations is that it is feasible to use the consistent mass matrix, as opposed to the lumped mass matrix, for the time integration of the governing equations of the fluid. This is because the inverse of the global consistent mass matrix can easily be directly assembled from the inverted consistent mass matrices of the elements, thus eliminating the need for lumping. This combination has also been shown to be stable and have good balance preserving properties (Cotter *et al.*, 2009). An upwind scheme is selected for the discretisation of advective boundary terms at element faces that are internal to Ω^h. The viscous boundary terms at these internal element faces are discretised using a compact discontinuous Galerkin scheme. Under these assumptions, the semi-discrete form of the balance of linear momentum can be written in matrix form as:

$$\mathbb{M}\frac{d\mathrm{u}}{dt} + \left(\mathbb{A}(\mathrm{u}) + \mathbb{K} + \mathbb{D}(\mathrm{u})\right)\mathrm{u} + \mathbb{C}\mathrm{p} = \mathrm{f_s} + \mathrm{f_t} + \mathrm{f_w}, \tag{10}$$

where u, p and $\mathrm{f_s}$ are column vectors containing the nodal values of the spatially discretised velocity, pressure and artificial body force, respectively. The matrices $\mathbb{M}$, $\mathbb{A}(\mathrm{u})$, $\mathbb{K}$ and $\mathbb{C}$ represent the mass matrix, the advection matrix evaluated at u, the diffusion matrix and the pressure gradient matrix, respectively. Details about the structure of these matrices can be found in Piggott *et al.* (2008). The coefficients obtained from the discretisation of the advective and viscous boundary terms at the internal element faces are stored in the matrix $\mathbb{D}(\mathrm{u})$. The column vectors $\mathrm{f_t}$ and $\mathrm{f_w}$ are associated with the traction and weak velocity boundary conditions, respectively. The semi-discrete continuity equation has the form:

$$\mathbb{C}^T\mathrm{u} = \mathrm{c}, \tag{11}$$

where c contains the contributions from the weak boundary conditions specified for **u**.

3.2 Penalty term

In addition to the mesh of $\mathbf{\Omega}$, the IB method requires the creation of a FE mesh of $\mathbf{\Omega}_\mathrm{s}$. The union of these elements form the domain $\mathbf{\Omega}_\mathrm{s}^h$ such that $\mathbf{\Omega}_\mathrm{s} \approx \mathbf{\Omega}_\mathrm{s}^h$. All fields on $\mathbf{\Omega}_\mathrm{s}^h$ are discretised using continuous piece-wise linear polynomials (P1). Furthermore, the penalty method makes use of two different discretisations of α_s. The first discretisation uses the same shape functions as **u** and will be denoted as $\alpha_{\mathrm{s},u}$. The second discretisation uses the shape functions of $\mathbf{\Omega}_\mathrm{s}^h$ and will be represented by $\alpha_{\mathrm{s,s}}$. If the structure is non-porous, $\alpha_{\mathrm{s,s}} = 1$ as $\mathbf{\Omega}_\mathrm{s}^h$ is filled entirely with solid material. *Fluidity* calculates $\alpha_{\mathrm{s},u}$ through a Galerkin projection of $\alpha_{\mathrm{s,s}}$ onto $\mathbf{\Omega}^h$:

$$\int_{\Omega^h} N_I(\mathbf{x})\alpha_{\mathrm{s},u}\ d\Omega = \int_{\Omega_\mathrm{s}^h} N_I(\mathbf{x})\alpha_{\mathrm{s,s}}\ d\Omega, \tag{12}$$

where N_I is the shape function of the node with global node number I from the discretisation of **u**. The total number of nodes in this discretisation will be denoted by n_u.

As with the solid concentration field, the velocity of the body $\mathbf{u}_\mathrm{s}$ is first discretised on $\mathbf{\Omega}_\mathrm{s}^h$ resulting in the field $\mathbf{u}_{\mathrm{s,s}}$. An alternative discretisation of $\mathbf{u}_{\mathrm{s},u}$, which is expressed using the same shape functions as **u**, is then obtained through the Galerkin projection of $\mathbf{u}_{\mathrm{s,s}}$ onto $\mathbf{\Omega}^h$. The column vector containing the nodal values of $\mathbf{u}_{\mathrm{s},u}$ will be denoted by $\mathrm{u}_{\mathrm{s},u}$. Further information about the Galerkin projection algorithm can be found in Farrell *et al.* (2009) and Farrell and Maddison (2011).

Replacing the continuous fields in equation (4) with their discretised counterparts leads to:

$$\mathrm{f_s} = \mathbb{Q}\mathrm{u}_{\mathrm{s},u} - \mathbb{P}\mathrm{u}, \tag{13}$$

where $\mathbb{P}$ and $\mathbb{Q}$ are block-diagonal matrices that each consist of $d \times d$ blocks, where d is the number of spatial dimensions. Each block is a sub-matrix of dimensions $n_u \times n_u$. All of the main diagonal blocks in $\mathbb{P}$ are identical, as are all of the main diagonal blocks of $\mathbb{Q}$. The entries of each main diagonal block in $\mathbb{P}$ and $\mathbb{Q}$ are given by:

$$\mathbb{P}_{IJ} = \beta \int_{\Omega^h} \alpha_{\mathrm{s},u} N_I(\mathbf{x}) N_J(\mathbf{x}) \; d\Omega \; , \tag{14}$$

$$\mathbb{Q}_{IJ} = \beta \int_{\Omega^h} N_I(\mathbf{x}) N_J(\mathbf{x}) \; d\Omega \; , \tag{15}$$

By defining $\mathbb{B} = \left(\mathbb{M} \frac{d}{dt} + \mathbb{A}(\mathrm{u}) + \mathbb{K} + \mathbb{D}(\mathrm{u}) \right)$, the semi-discrete governing equations of the penalty method can be written compactly in block matrix form as:

$$\begin{bmatrix} \mathbb{B} + \mathbb{P} & \mathbb{C} \\ \mathbb{C}^T & 0 \end{bmatrix} \begin{bmatrix} \mathrm{u} \\ \mathrm{p} \end{bmatrix} = \begin{bmatrix} \mathrm{f_t} + \mathrm{f_w} + \mathbb{Q}\mathrm{u}_{\mathrm{s},u} \\ \mathrm{c} \end{bmatrix}. \tag{16}$$

3.3 Lagrange multiplier term

The Lagrange multiplier field $\boldsymbol{\lambda}$ can be discretised by either regularising it to a mesh of the overall domain, such as Ω^h, (Peskin (1972), Taira and Colonius (2007) and Lācis *et al.* (2016)) or by representing it on a mesh of Ω_s, such as Ω_s^h (Glowinski *et al.* (1998), Kadapa *et al.* (2016) and Boffi and Gastaldi (2017)). For definiteness, the latter approach is implemented in the present work, a task that is facilitated because of the fact that *Fluidity* is already configured to generate a mesh Ω_s^h of Ω_s for the IB method. The column vector containing the nodal values of $\boldsymbol{\lambda}$ will be denoted by l. Replacing each of the quantities in equation (6) with their discretised versions and substituting in $\alpha_{\mathrm{s,s}} = 1$ results in:

$$\mathrm{f_s} = \mathbb{L}\mathrm{l}. \tag{17}$$

Similarly, the discretised version of the weak form of the no-slip condition is:

$$\mathbb{L}^T \mathrm{u} = \mathbb{S}\mathrm{u}_{\mathrm{s,s}}. \tag{18}$$

The matrices $\mathbb{L}$ and $\mathbb{S}$ are both block diagonal consisting of $d \times d$ blocks, with all of the main diagonal blocks being identical. Each main diagonal block of $\mathbb{L}$ has dimensions $n_u \times n_\mathrm{s}$, where n_s is the total number of nodes in Ω_s^h. The entries of each of these blocks of $\mathbb{L}$ are given by:

$$\mathbb{L}_{IJ} = \int_{\Omega_\mathrm{s}^h} N_I M_J \; d\Omega \; . \tag{19}$$

where M_J is the shape function associated with the node with global node number J from Ω_s^h. Each main diagonal block of $\mathbb{S}$ has the dimensions of $n_\mathrm{s} \times n_\mathrm{s}$ and is simply the mass matrix of Ω_s^h. The entries of each main diagonal block of $\mathbb{S}$ are, therefore:

$$\mathbb{S}_{IJ} = \int_{\Omega_\mathrm{s}^h} M_I M_J \; d\Omega \; . \tag{20}$$

The governing equations of the Lagrange multiplier method can be expressed in block matrix form as:

$$\begin{bmatrix} \mathbb{B} & \mathbb{C} & \mathbb{L} \\ \mathbb{C}^T & 0 & 0 \\ \mathbb{L}^T & 0 & 0 \end{bmatrix} \begin{bmatrix} \mathrm{u} \\ \mathrm{p} \\ \mathrm{l} \end{bmatrix} = \begin{bmatrix} \mathrm{f_t} + \mathrm{f_w} \\ \mathrm{c} \\ \mathbb{S}\mathrm{u_{s,s}} \end{bmatrix}. \tag{21}$$

3.4 Effect on traction calculation

As the discretised domain $\boldsymbol{\Omega}^h$ does not conform to the shape of $\partial\boldsymbol{\Omega}_\mathrm{s}$, it does not capture $\partial\boldsymbol{\Omega}_\mathrm{s}$ as a sharp interface (Viré *et al.*, 2015). As explained by Viré *et al.* (2015), this causes the stagnation points of the flow field to not be located on $\partial\boldsymbol{\Omega}_\mathrm{s}$ as they should, but shifts them a distance of approximately l_e away from it. During the post-processing of the discretised flow field, selecting $\partial\boldsymbol{\Omega}_\mathrm{s}$ as the curve along, which to calculate the resultant traction can, therefore cause significant errors as it may not adequately capture the stagnation points. To compensate for this effect, a surrogate solid domain $\boldsymbol{\Omega}_\mathrm{s}^*$ is introduced. The boundary of this surrogate domain, $\partial\boldsymbol{\Omega}_\mathrm{s}^*$, is then used when post-processing the traction resulting in:

$$\mathbf{t} = \int_{\partial\Omega_\mathrm{s}^*} \boldsymbol{\sigma}(\mathbf{x}, \mathrm{t})\mathbf{n}_\mathrm{s}^*(\mathbf{x}, t) \; dS, \tag{22}$$

where $\mathbf{n}_\mathrm{s}^*(\mathbf{x}, t)$ is a unit vector that is normal to $\partial\boldsymbol{\Omega}_\mathrm{s}^*$ and points out of $\boldsymbol{\Omega}_\mathrm{s}^*$. The surrogate domain is generated by displacing each point on $\partial\boldsymbol{\Omega}_\mathrm{s}$ perpendicularly outward by a distance of l_e.

4. Time discretisation

4.1 Penalty approach

The governing equations of the fluid are integrated in time using a predictor-corrector method (Piggott *et al.*, 2008; Viré *et al.*, 2012). For the penalty approach, the time-discretised balance of linear momentum (equation (10)) is:

$$\mathbb{M}\frac{\tilde{\mathrm{u}}^{n+1} - \mathrm{u}^n}{\Delta t} + \left(\mathbb{A}(\tilde{\mathrm{u}}^{n+\theta}) + \mathbb{K} + \mathbb{D}(\tilde{\mathrm{u}}^{n+\theta})\right)\tilde{\mathrm{u}}^{n+\theta} + \mathbb{P}^n\tilde{\mathrm{u}}^{n+\theta} = \mathrm{f}^{n+1}, \tag{23a}$$

$$\mathrm{f}^{n+1} = \mathrm{f}_\mathrm{t}^{n+1} + \mathrm{f}_\mathrm{w}^{n+1} + \mathbb{Q}\mathrm{u}_{\mathrm{s},u}^n - \mathbb{C}\tilde{\mathrm{p}}^{n+1}, \tag{23b}$$

where the superscript denotes the time at which the variable is being evaluated, e.g. $\mathrm{u}^n = \mathrm{u}(n\Delta t)$ or $\mathrm{u}^{n+1} = \mathrm{u}((n+1)\Delta t)$, with Δt being the integration time step. This superscript is omitted for quantities that are constant with respect to time, e.g. $\mathbb{M}$ or $\mathbb{C}$. The term $\tilde{\mathrm{u}}^{n+\theta}$ is defined by:

$$\tilde{\mathrm{u}}^{n+\theta} = \theta\tilde{\mathrm{u}}^{n+1} + (1-\theta)\mathrm{u}^n, \tag{24}$$

with $\theta = 0.5$ corresponding to the Crank-Nicolson scheme. The predictor step consists of specifying a candidate value for the pressure field $\tilde{\mathrm{p}}^{n+1}$ and then solving equations (23a) and (23b) to find a candidate velocity field $\tilde{\mathrm{u}}^{n+1}$. The corrector step consists of first solving the following Poisson problem for the pressure correction $(\mathrm{p}^{n+1} - \tilde{\mathrm{p}}^{n+1})$ so that the continuity equation (equation (11)) is satisfied:

$$\Delta t \mathbb{C}^T \mathbb{M}^{-1} \mathbb{C} \left(\mathrm{p}^{n+1} - \tilde{\mathrm{p}}^{n+1} \right) = \mathbb{C}^T \tilde{\mathrm{u}}^{n+1} - \mathrm{c}^{n+1}. \tag{25}$$

The value of the pressure field p^{n+1} is obtained by simply applying this correction to $\tilde{\mathrm{p}}^{n+1}$. Once the pressure correction is known, the velocity field u^{n+1} is calculated:

$$\mathrm{u}^{n+1} = \tilde{\mathrm{u}}^{n+1} + \Delta t \mathbb{M}^{-1} \mathbb{C} \left(\mathrm{p}^{n+1} - \tilde{\mathrm{p}}^{n+1} \right). \tag{26}$$

At the beginning of each time-step, the value of $\tilde{\mathrm{p}}^{n+1}$ is set equal to p^n. The predictor-corrector method is then executed and repeated, if necessary, until the changes in p^{n+1} and u^{n+1} between consecutive sub-iterations are sufficiently small.

4.2 Lagrange multiplier approach

To provide a fair comparative analysis, the time integration scheme used by the Lagrange multiplier approach is simply an extension of the predictor-corrector method used by the penalty approach. The time discretised version of equation (10) is thus, also similar:

$$\mathbb{M} \frac{\tilde{\mathrm{u}}^{n+1} - \mathrm{u}^n}{\Delta t} + \left(\mathbb{A}\left(\tilde{\mathrm{u}}^{n+\theta}\right) + \mathbb{K} + \mathbb{D}\left(\tilde{\mathrm{u}}^{n+\theta}\right) \right) \tilde{\mathrm{u}}^{n+\theta} = \mathrm{f}^{n+1} \tag{27a}$$

$$\mathrm{f}^{n+1} = \mathrm{f}_{\mathrm{t}}^{n+1} + \mathrm{f}_{\mathrm{w}}^{n+1} - \mathbb{C} \tilde{\mathrm{p}}^{n+1} - \mathbb{L}^n \tilde{\mathrm{l}}^{n+1}. \tag{27b}$$

The procedure for solving $\tilde{\mathrm{u}}^{n+1}$ is the same as that adopted in the penalty approach, except that now candidate values have to be provided for both $\tilde{\mathrm{p}}^{n+1}$ and $\tilde{\mathrm{l}}^{n+1}$. Furthermore, in the corrector step, the Lagrange multiplier field correction $\left(\mathrm{l}^{n+1} - \tilde{\mathrm{l}}^{n+1} \right)$ is first computed, such that the no-slip condition (equation (18)) is enforced, by solving:

$$\Delta t \left(\mathbb{L}^T \right)^n \mathbb{M}^{-1} \mathbb{L}^n \left(\mathrm{l}^{n+1} - \tilde{\mathrm{l}}^{n+1} \right) = \left(\mathbb{L}^T \right)^n \tilde{\mathrm{u}}^{n+1} - \mathbb{S}^T \mathrm{u}_{\mathrm{s,s}}^n. \tag{28}$$

The value of l^{n+1} is then obtained by applying this correction to $\tilde{\mathrm{l}}^{n+1}$. With l^{n+1} known, the pressure correction $\left(\mathrm{p}^{n+1} - \tilde{\mathrm{p}}^{n+1} \right)$ is then calculated, such that the continuity equation (equation (11)) is satisfied, by solving:

$$\Delta t \mathbb{C}^T \mathbb{M}^{-1} \mathbb{C} \left(\mathrm{p}^{n+1} - \tilde{\mathrm{p}}^{n+1} \right) = \mathbb{C}^T \tilde{\mathrm{u}}^{n+1} - \mathrm{c}^{n+1} - \Delta t \mathbb{C}^T \mathbb{M}^{-1} \mathbb{L}^n \left(\mathrm{l}^{n+1} - \tilde{\mathrm{l}}^{n+1} \right). \tag{29}$$

Finally, u^{n+1} is computed using:

$$\mathrm{u}^{n+1} = \tilde{\mathrm{u}}^{n+1} + \Delta t \mathbb{M}^{-1} \mathbb{C} \left(\mathrm{p}^{n+1} - \tilde{\mathrm{p}}^{n+1} \right) + \Delta t \mathbb{M}^{-1} \mathbb{L}^n \left(\mathrm{l}^{n+1} - \tilde{\mathrm{l}}^{n+1} \right). \tag{30}$$

At the start of each time-step, $\tilde{\mathrm{p}}^{n+1}$ and $\tilde{\mathrm{l}}^{n+1}$ are set equal to p^n and l^n, respectively. As in the penalty approach, the predictor-corrector method is repeated, if necessary, until the changes in p^{n+1}, l^{n+1} and u^{n+1} are sufficiently small between consecutive sub-iterations.

4.3 Governing equations of the structure and fluid-structure interaction coupling

The trapezoidal rule is used to discretise equation (8) in time resulting in:

$$m\bar{a}_1^{n+1} + c\bar{u}_1^{n+1} + k\bar{x}_1^{n+1} = \bar{t}_1^{n+1}, \tag{31a}$$

$$\bar{u}_1^{n+1} = \bar{u}_1^n + \frac{\Delta t}{2}\left(\bar{a}_1^n + \bar{a}_1^{n+1}\right), \tag{31b}$$

$$\bar{x}_1^{n+1} = \bar{x}_1^n + \Delta t\bar{u}_1^n + \frac{(\Delta t)^2}{4}\left(\bar{a}_1^n + \bar{a}_1^{n+1}\right). \tag{31c}$$

Equations (31b) and (31c) are used to eliminate $\bar{u}_1^{n+1}$ and $\bar{x}_1^{n+1}$ from equation (31a). A Newton-Raphson method is then used to solve the resulting equation for $\bar{a}_1^{n+1}$, after which $\bar{u}_1^{n+1}$ and $\bar{x}_1^{n+1}$ are calculated using equations (31b) and (31c), respectively, via back-substitution. These operations are performed using a separate rigid body dynamics code.

During each time step of a simulation, the governing equations of the fluid are first solved to obtain the updated velocity and pressure fields, u^{n+1} and p^{n+1}, respectively. From this, the new traction $\bar{\mathbf{t}}^{n+1}$ is computed and applied to the structure. The rigid body dynamics code then solves equation (31a) through equation (31c) for the updated position $\bar{x}_1^{n+1}$ and velocity $\bar{u}_1^{n+1}$ of the centre of gravity of the structure. Finally, from this, the new velocity field $u_{s,s}$ of the structure is calculated from the computational fluid dynamics (CFD) code, and the position of its mesh Ω_s^h is updated, after which the next time step is initiated.

5. Comparative analysis

In this section, the results obtained using the penalty and the Lagrange multiplier approaches are compared for three test problems, namely, the laminar flow through a channel, the harmonic motion of cylinder through a stationary fluid, and the vortex-induced vibration of a cylinder.

5.1 Channel flow

Figure 2 presents the domain used to simulate the laminar flow of an incompressible Newtonian fluid through a channel. The penalty and Lagrange multiplier approaches are each used to create a channel, denoted by Ω_f, of width $2L$. This is done by imposing the constraint $\mathbf{u} = \mathbf{0}$ within $\Omega_s = \Omega_{s,1} \cup \Omega_{s,r}$ (the shaded regions). The walls of the resulting channel, which should be located at $x = \pm L$, are denoted by $\partial\Omega_{s,1}$ and $\partial\Omega_{s,r}$. An analytical solution can be derived for fully developed steady flow with inlet and outlet pressures of p_i and p_o, respectively. The velocity field $\mathbf{u}_{ss}$ and pressure field p_{ss} from the steady-state analytical solution, for a channel of width $2L$ and length $4L$, are given by:

$$\mathbf{u}_{ss}(\mathbf{x}) = \frac{p_i - p_o}{8\mu L}\left(x_1^2 - L^2\right)\mathbf{e}_2, \tag{32a}$$

$$p_{ss}(\mathbf{x}) = \frac{p_i - p_o}{4L}(x_2 + 2L) + p_o. \tag{32b}$$

As shown in Figure 2, an inlet velocity profile consisting of $\mathbf{u} = \mathbf{u}_{ss}$ within the interval $|x_1| \leq L$ and $\mathbf{u} = \mathbf{0}$ outside of it, is applied to the top domain boundary. A boundary condition of $\boldsymbol{\sigma}\mathbf{n} = -p_o\mathbf{n}$ is applied to the bottom boundary. Initially, $\mathbf{u} = \mathbf{0}$ and $p = p_o$ throughout the entire domain. After a sufficient amount of time has passed, the flow field inside of Ω_f should reach a steady-state in which $\mathbf{u} = \mathbf{u}_{ss}$ and $p = p_{ss}$.

The penalty and Lagrange multiplier approaches are used to simulate the case in which $p_i = 400$ Pa, $p_o = 0$ Pa, $L = 1$ m, $\rho = 1$ kg/m^3 and $\mu = 1$ kg/ms. This results in a Reynolds number

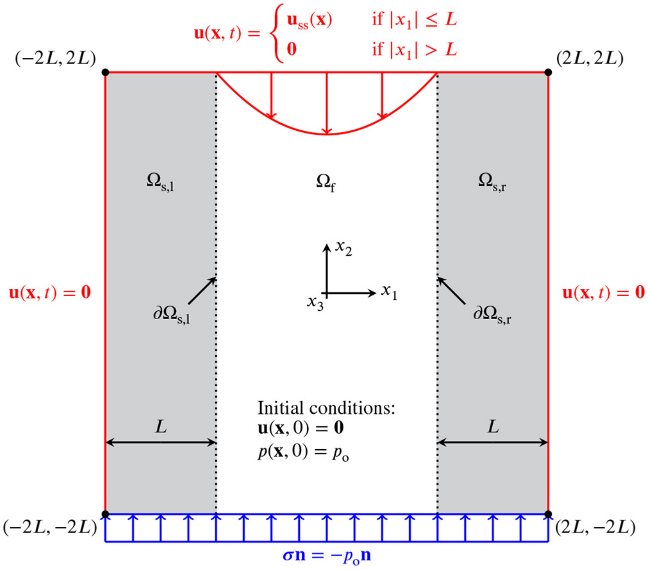

Figure 2.
Domain for simulating the laminar flow of an incompressible Newtonian fluid through a channel

Note: The penalty and Lagrange multiplier approaches are used to create a channel of width 2 L. In each case, this is done by using the artificial body force $\mathbf{f}_s$ to enforce the constraint $\mathbf{u} = \mathbf{0}$ within $\Omega = \Omega_{s,1} \cup \Omega_{s,r}$ (the shaded regions). At the top boundary $\mathbf{u} = \mathbf{u}_{ss}$, with $\mathbf{u}_{ss}$ being the velocity field from the analytical solution for fully developed steady flow. A constant outlet pressure p_o is prescribed at the bottom boundary

of $Re = \rho\,(p_i - p_o)L^2/(4\mu^2) = 66.7$. Each simulation is run for $300\Delta t$ at $\Delta t = 0.001$ s. Four different computational meshes are considered. The so-called "very coarse" and "coarse" meshes have 1,022 and 4,320 elements, respectively. For the "very coarse" mesh, $l_e/L = 1/5$ throughout the entire domain, where l_e is the local element edge length. Similarly, $l_e/L = 1/10$ throughout the entire domain for the "coarse" mesh. Two additional meshes, which will be referred to as "intermediate" and "fine", are generated by refining the coarse mesh near $\partial\Omega_{s,1}$ and $\partial\Omega_{s,r}$. For the intermediate mesh, which is shown in Figure 3, zones of finer elements with $l_e/L = 1/40$ are created on both sides of $\partial\Omega_{s,1}$ and $\partial\Omega_{s,r}$. The edge length increases with the distance from these zones so that $l_e/L = 1/10$ at the channel centreline and at the side boundaries of the domain. This results in a mesh of 17,184 elements. The fine mesh is constructed in the same manner except that $l_e/L = 1/100$ in the zones of finer elements near $\partial\Omega_{s,1}$ and $\partial\Omega_{s,r}$, producing a mesh of 53,411 elements. In addition, simulations with the penalty method are conducted for three values of the penalty factor: $\beta = \beta^*/10$, β^* and $10\beta^*$. The value of β^* is determined using the following formula that is recommended for the IB method:

$$\beta^* = \max\left(\frac{\rho}{\Delta t}, \frac{\mu}{l_{e,\min}^2}\right), \tag{33}$$

where $l_{e,\min}$ is the minimum value of l_e for the mesh being used (Viré *et al.*, 2012). Nine simulations were therefore, executed using the penalty approach.

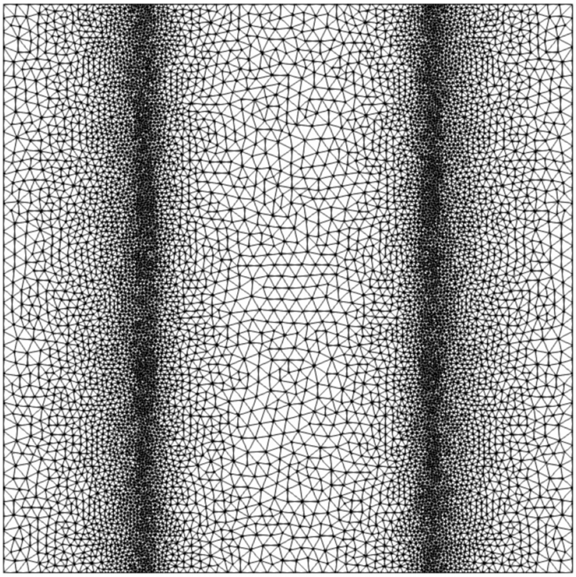

Figure 3. The intermediate version of the computational mesh Ω^h of the overall domain $\boldsymbol{\Omega}$, used to simulate the steady laminar flow of an incompressible Newtonian fluid through a channel

The component u_2, in the x_2-direction, of $\mathbf{u}$ computed at the bottom boundary using the intermediate mesh is plotted in Figure 4(a) at $t = 150\Delta t$. This value of t is selected for the plots as it was found that all of the solutions had reached steady-state by this time. Figure 4(b) shows the steady-state pressure at the centreline of the channel. Both the penalty method with $\beta = 10\beta^*$ and the Lagrange multiplier method predict profiles for the velocity and the pressure that agree very closely with the analytical solution. The velocity profiles calculated by the penalty method with $\beta = \beta^*/10$ and $\beta = \beta^*$ overpredict the minimum velocity and exhibit a non-zero velocity at walls of the channel. Therefore, in these two cases, a significant amount of fluid is leaking into $\boldsymbol{\Omega}_{\mathrm{s}}$. This is confirmed by the pressure profiles for these two cases, which both underpredict the pressure drop across the channel. The solution obtained by the penalty method is therefore, more accurate with $\beta = 10\beta^*$ than with the recommended value of β^*, which shows that the appropriate value for β can be difficult to determine a priori.

To examine the numerical solutions in more detail, the quantity r^*_{ss} is defined as the L^2-norm of the error in $\mathbf{u}$ relative to $\mathbf{u}_{\mathrm{ss}}$, calculated over a region $\boldsymbol{\Omega}^*$ and non-dimensionalised using the L^2-norm of $\mathbf{u}_{\mathrm{ss}}$ over this region:

$$r^*_{\mathrm{ss}}(\Omega^*) = 100\% \times \sqrt{\frac{\int_{\Omega^*} \left(||\mathbf{u} - \mathbf{u}_{\mathrm{ss}}||_2\right)^2 \, d\Omega}{\int_{\Omega^*} \left(||\mathbf{u}_{\mathrm{ss}}||_2\right)^2 \, d\Omega}}. \tag{34}$$

Similarly, $r^*_{\mathrm{p,ss}}$ is the L^2-norm of the error in p relative to p_{ss}, calculated over $\boldsymbol{\Omega}^*$ and non-dimensionalised using the L^2-norm of p_{ss} over this region:

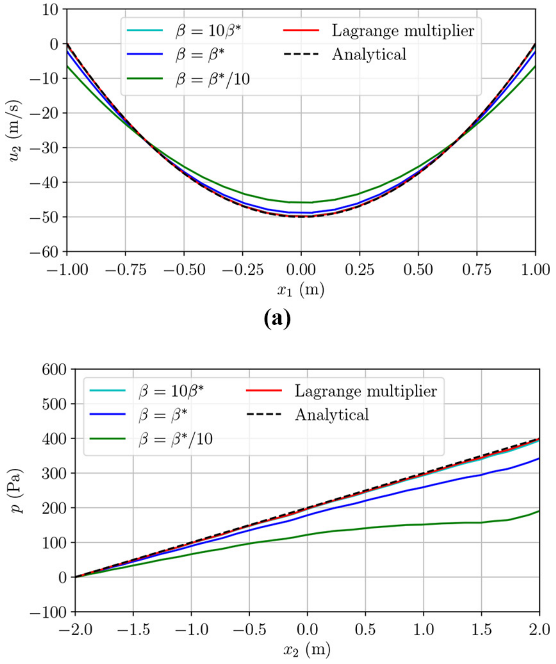

(a)

(b)

Figure 4.
Shown in (a) is the component u_2, in the x_2-direction, of the velocity at the outlet of the channel and (b) presents the pressure p along the channel centreline

Notes: In both (a) and (b), the profiles are obtained using the Lagrange multiplier and penalty methods after the flow field has reached steady-state. The profiles from the penalty method are plotted for three penalty factors: $\beta = \beta^*/10$, β^* and $10\beta^*$, where β^* is the recommended penalty factor. Also show is the steady-state analytical solution

$$r^*_{p,\mathrm{ss}}(\Omega^*) = 100\% \times \sqrt{\frac{\int_{\Omega^*} \left(\|p - p_{\mathrm{ss}}\|_2\right)^2 \, d\Omega}{\int_{\Omega^*} \left(\|p_{\mathrm{ss}}\|_2\right)^2 \, d\Omega}}. \tag{35}$$

The values of $r^*_{\mathrm{ss}}(\Omega_{\mathrm{f}})$ and $r^*_{\mathrm{ss}}(\Omega_{\mathrm{s}})$ are plotted in Figures 5(a) and 5(b), respectively, for the very coarse, coarse, intermediate and fine meshes. The value of $r^*_{\mathrm{ss}}(\Omega_{\mathrm{s}})$ is calculated by letting $\mathbf{u}_{\mathrm{ss}} = \mathbf{0}$ in Ω_{s}, and therefore, represents the error with which the no-slip condition is imposed. Likewise, $r^*_{p,\mathrm{ss}}(\Omega_{\mathrm{f}})$ is plotted for each of these meshes in Figure 6. According to Figure 5(a), the velocity field from the Lagrange multiplier method exhibits the least error inside of Ω_{f} on all four meshes. Out of the penalty factors tested, $\beta = \beta^*$ results in the lowest error inside of Ω_{f} on the very coarse and coarse meshes. However, it is surpassed by $\beta = 10\beta^*$ on the medium and fine meshes. Figure 5(b) shows that the Lagrange multiplier method also enforces the no-slip condition the most accurately on the coarse, medium and

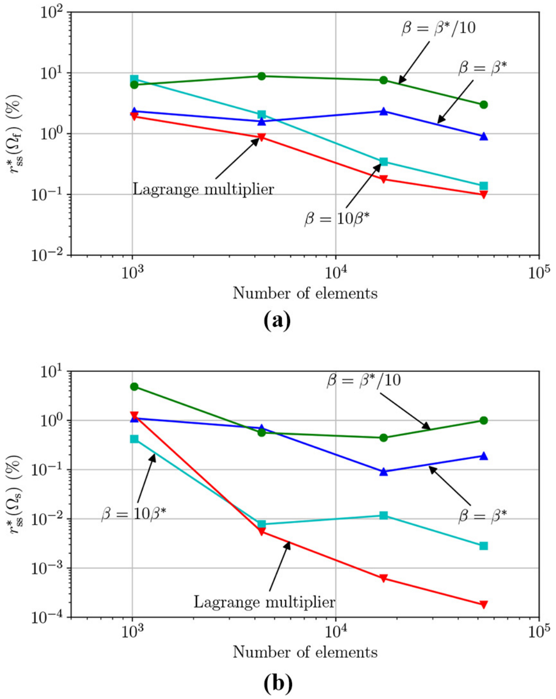

Notes: It is plotted in (a) for $\Omega^* = \Omega_\mathrm{f}$ (inside of the channel) and in (b) for $\Omega^* = \Omega_\mathrm{s}$ (inside of the walls). In both (a) and (b), the data is plotted as a function of the number elements in the computational mesh of the overall domain $\Omega = \Omega_\mathrm{s} \cup \Omega_\mathrm{f}$

Figure 5.
The non-dimensionalised error $r^*_{\mathrm{ss}}(\Omega^*)$ in the steady-state velocity, with respect to the analytical solution and calculated over the region Ω^*, is shown for the Lagrange multiplier method and the penalty method for penalty factors $\beta = \beta^*/10, \beta^*$ and $10\beta^*$, where β^* is the recommended penalty factor

fine meshes, but is actually surpassed slightly on the very coarse mesh by the penalty method with $\beta = \beta^*$. Similarly, when looking at $r^*_{\mathrm{p,ss}}(\Omega_\mathrm{f})$, the Lagrange multiplier method is surpassed narrowly by the penalty method with $\beta = \beta^*$ on the very coarse mesh and again with $\beta = 10\beta^*$ on the fine mesh. As expected, $r^*_{\mathrm{ss}}(\Omega_\mathrm{f})$, $r^*_{\mathrm{ss}}(\Omega_\mathrm{s})$ and $r^*_{p,\mathrm{ss}}(\Omega_\mathrm{f})$ from the Lagrange multiplier method all decrease monotonically as the mesh is refined. For both $r^*_{\mathrm{ss}}(\Omega_\mathrm{f})$ and $r^*_{p,\mathrm{ss}}(\Omega_\mathrm{f})$, the Lagrange multiplier method shows approximately linear convergence with respect to the number of elements. For $r^*_{\mathrm{ss}}(\Omega_\mathrm{s})$, the rate of convergence of the Lagrange multiplier method is greater than linear from the very coarse mesh to the coarse mesh, but then also becomes approximately linear as the mesh is successively refined. However, the penalty method does not necessarily exhibit this monotonic decrease in these quantities. This behaviour is possibly because of the max $(\cdot, \cdot)$ operator in equation (33). For the very coarse and coarse meshes, the term $\rho/\Delta t$ is the largest, and is thus, used to define β^*. However, when moving to the intermediate mesh, the term $\mu/l^2_{\mathrm{e,min}}$ becomes the largest, hence changing this definition. Nevertheless, for the Lagrange multiplier method, and for the penalty method with $\beta = \beta^*$ and $\beta = 10\beta^*$, the values of $r^*_{\mathrm{ss}}(\Omega_\mathrm{f})$, $r^*_{\mathrm{ss}}(\Omega_\mathrm{s})$ and $r^*_{p,\mathrm{ss}}(\Omega_\mathrm{f})$ all only change a small amount, less than 2%, 1% and 1%, respectively, between the intermediate and fine meshes indicating convergence with respect to mesh refinement. As with the Lagrange multiplier method, the penalty method with

$\beta = 10\beta^*$ exhibits approximately linear convergence in $r^*_{ss}(\Omega_f)$ and $r^*_{p,ss}(\Omega_f)$ as the mesh is refined. However, for $r^*_{ss}(\Omega_s)$, the rate of convergence for $\beta = 10\beta^*$ drops dramatically with refinement beyond the coarse mesh. Furthermore, for the intermediate and fine meshes, $r^*_{ss}(\Omega_f)$, $r^*_{ss}(\Omega_s)$ and $r^*_{p,ss}(\Omega_f)$ all decrease as β is increased. This indicates that it is difficult to find a priori a suitable value for the penalty factor β.

Finally, Figure 7 presents the computational times required by the Lagrange multiplier and penalty methods to reach various thresholds in $r^*_{ss}(\Omega_f)$, i.e. to get to within a certain error of steady-state, when using the intermediate mesh. The thresholds selected for this comparison were $r^*_{ss}(\Omega_f) = 0.1\ \%, 0.5\ \%, 1\ \%, 5\ \%$ and $10\ \%$. For the penalty method, the crosses indicate the lowest threshold that could be achieved using that value of β.

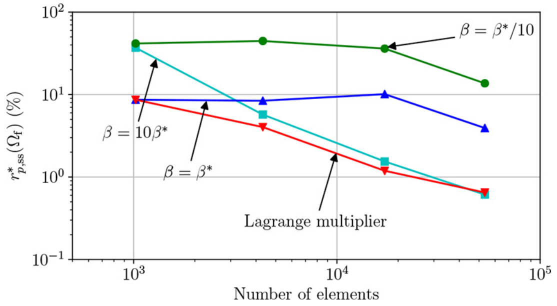

Figure 6. The non-dimensionalised error $r^*_{p,ss}(\Omega^*)$ in the steady-state pressure, with respect to the analytical solution and calculated over the region Ω_f (inside of the channel), is shown for the Lagrange multiplier method and the penalty method for penalty factors $\beta = \beta^*/10$, β^* and $10\beta^*$, where β^* is the recommended penalty factor

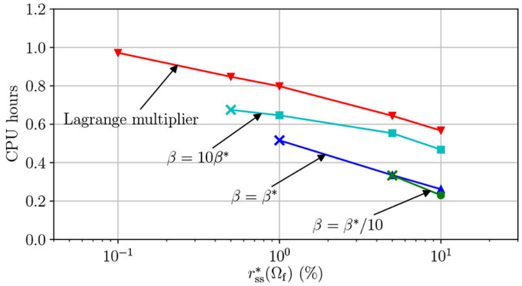

Figure 7. Computational times for the Lagrange multiplier method and the penalty method for penalty factors $\beta = \beta^*/10$, β^* and $10\beta^*$, where β^* is the recommended penalty factor, obtained using the intermediate mesh

Notes: Each computational time shown is the total CPU hours required by the solver to produce a velocity field inside the channel that is within a certain threshold of the steady-state solution. The times are plotted for the thresholds $r^*_{ss}(\Omega_f) = 0.1\%$, 0.5%, 1%, 5% and 10%

The computational time for the penalty method is that which is needed to solve the balance of linear momentum and the pressure correction equation, summed over all non-linear iterations per time step, and all time steps up until $r^*_{ss}(\Omega_f)$ reaches the specified threshold. The computational time is calculated in the same manner for the Lagrange multiplier method, except that the time needed to solve the Lagrange multiplier correction equation (equation (28)) is also included. The results in Figure 7, which shows that the Lagrange multiplier method is computationally more expensive than the penalty method for all of the cases simulated. This is explained by the fact that, unlike the penalty method, the Lagrange multiplier method executes additional operations when solving the Lagrange multiplier field. However, Figure 7 does show that computational time spent by the penalty method increases as the penalty factor is raised. This is caused by the penalty term deteriorating the convergence rate of both the solver of the pressure correction and the non-linear iterations. Consequently, these results indicate that, for the same accuracy, the Lagrange multiplier method generally requires similar or additional computational time compared to the penalty method, but it is more robust in the sense that it does not require calibration (i.e. it does not use a penalty parameter). Furthermore, only the Lagrange multiplier method is able to reach the threshold of $r^*_{ss}(\Omega_f) = 0.1\ \%$. This agrees with the errors plotted in Figures 5(a) and 5(b) that demonstrated that the Lagrange multiplier method is able to get closer to the analytical solution than the penalty method.

5.2 Harmonic motion of a cylinder through a stationary fluid

This test problem considers the harmonic motion of a cylinder that is immersed in a stationary incompressible fluid (Dütsch *et al.*, 1998). The computational domain is illustrated in Figure 8 and has dimensions of $55D \times 35D$, where D is the diameter of the cylinder. The cylinder executes the prescribed translational motion of period T defined by $x_1(t) = -A \sin(2\pi t/T)$. As indicated in Figure 8, the computational mesh featured a rectangular region of finer elements of dimension $7D \times 4D$, centred about the origin. “Coarse”, “intermediate” and “fine” versions of this mesh are created that have values of l_e/D = 1/20, 1/40 and 1/80,

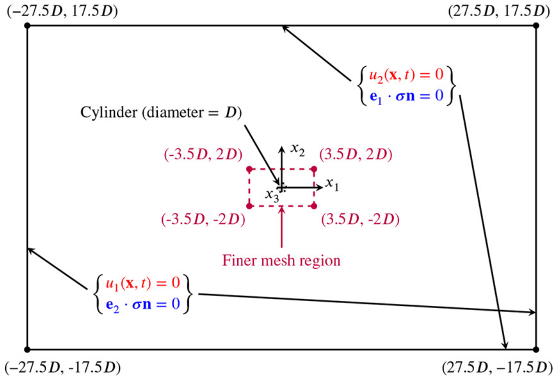

Note: The cylinder is initially located at the origin and executes the prescribed translation $\bar{\mathrm{x}}(t) = -A \sin(2\pi t/T)\mathrm{e}_1$, where $\mathbf{x}$ is the location of the centre of gravity of the cylinder and A and T are the amplitude and period of its motion, respectively

Figure 8. Computational domain to simulate the harmonic motion of a cylinder of diameter D that is immersed in a stationary, incompressible Newtonian fluid

respectively, in the finer region. The finer region is surrounded by a zone of coarser elements, in which l_e/D gradually increases to a value of 1 at the domain boundary. The "intermediate" mesh is illustrated in Figure 9.

The penalty and Lagrange multiplier approaches are used to simulate a Reynolds number of $Re = \rho(2\pi A/T)D/\mu = 100$ and a Keulegan-Carpenter number of $KC = 2\pi A/D = 5$. Simulations on the intermediate mesh are conducted for $\Delta t = T/50$, $T/100$ and $T/250$. A time-step of $\Delta t = T/100$ is used for simulations on the coarse and fine meshes. For each combination of mesh resolution and time-step, the simulations with the penalty method are executed for $\beta = \beta^*/10$, β^* and $10\beta^*$, with β^* being calculated from equation (33). In total, 15 simulations were, therefore, performed using the penalty method. In all of the simulations, the flow field becomes periodic after approximately $t = 4T$.

Figure 10 shows the component $\bar{t}_1^*$ of the non-dimensionalised traction $\bar{\mathbf{t}}^*$, which is defined by:

$$\bar{\mathbf{t}}^* = \frac{1}{\rho D}\left(\frac{T}{2\pi A}\right)^2 \bar{\mathbf{t}}, \tag{36}$$

Also shown is a reference solution from Dütsch *et al.* (1998) that was calculated using a DB method. The curves calculated for $\bar{t}_1^*$ by the penalty method with $\beta = 10\beta^*$ and Lagrange multiplier method are very similar and are closest to the reference solution. In contrast, the curve for $\beta = \beta^*$ (the recommended penalty factor) deviates appreciably from the reference solution. Contours of the non-dimensionalised component r^*, of the fluid velocity in the x_1-direction relative to that of the cylinder, are plotted in Figure 11 and show why $\bar{\mathbf{t}}^*$ obtained with $\beta = \beta^*$ does not match that from the reference solution. The value of r^* is defined by:

$$r^*(\mathbf{x}, t) = 100\% \times \frac{u_1(\mathbf{x}, t) - \bar{u}_1(t)}{\bar{u}_1(t)}. \tag{37}$$

The white circles in Figures 11(a) and 11(b) each represent the wetted boundary of the cylinder $\partial\Omega_s$. The white elements are from the solid mesh Ω_s^h. For the no-slip condition to be enforced exactly, r^* should be zero throughout Ω_s^h. Figure 11(a) shows that the Lagrange multiplier method almost achieves this condition, however, r^* does exhibit small oscillations about zero in this region. In contrast, when $\beta = \beta^*$ an appreciable amount of fluid is able to cross $\partial\Omega_s$ causing a large error in $\bar{\mathbf{t}}^*$.

Figure 9.
Presented in (a) is the intermediate version of the computational mesh Ω^h of the overall domain Ω, used to simulate the harmonic motion of a cylinder immersed in a stationary, incompressible Newtonian fluid. The mesh Ω^h has a finer region of elements at its center, denoted in green. A closeup of the region enclosed by the pink rectangle is shown in (b)

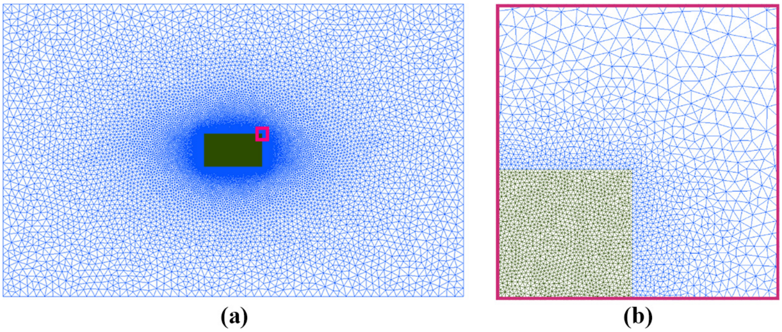

To study $\bar{\mathbf{t}}^*$ in more detail, the following ratio between the root mean square (RMS) of $\left(\bar{t}_1^* - \tilde{t}_1^*\right)$ and the RMS of $\tilde{t}_1^*$ is defined:

$$r_{\mathrm{t}}^* = 100\% \times \sqrt{\frac{\displaystyle\int_{kT}^{(k+1)T} \left(\bar{t}_1^* - \tilde{t}_1^*\right)^2 dt}{\displaystyle\int_{kT}^{(k+1)T} \left(\tilde{t}_1^*\right)^2 dt}}, \qquad k \geq 4, \tag{38}$$

where $\tilde{t}_1^*$ is the component, acting in the x_1-direction, of $\tilde{\mathbf{t}}^*$ from the reference solution. The quantity r_{t}^* is, therefore, an aggregate of the difference between $\bar{t}_1^*$ and $\tilde{t}_1^*$. Figure 12(a) plots r_{t}^* for the coarse, intermediate and fine meshes and $\Delta t = T/100$. Similarly, Figure 12(b) depicts r_{t}^* as a function of $\Delta t/T$, as calculated on the intermediate mesh. In both Figures 12(a) and 12(b), r_{t}^* from the Lagrange multiplier method is the lowest, except for when the fine mesh is used together with $\Delta t = T/100$. For the fine mesh and $\Delta t = T/100$, r_{t}^* for $\beta = 10\beta^*$ actually drops below that of the Lagrange multiplier method by approximately 1.5%. Similarly, when $\Delta t = T/250$ and $\Delta t = T/100$ are used together with the intermediate mesh, the values of r_{t}^* for $\beta = \beta^*$ and $\beta = 10\beta^*$ both approach those of the Lagrange multiplier method within about 1%. This corresponds with the findings of the channel flow test problem in Section 5.1, which suggested that the penalty method could approach the accuracy of the Lagrange multiplier method, when using the appropriate value of β.

In Figure 12(a), the curve from the Lagrange multiplier method only drops a maximum of approximately 2% between consecutive meshes as Ω^h is refined. The solutions from the Lagrange multiplier method are, therefore, similar on all three meshes. The curve for $\beta = 10\beta^*$ decreases by about 3% when progressing from the coarse mesh to the medium mesh, and a further 9% when moving to the fine mesh. These decreases are larger than those

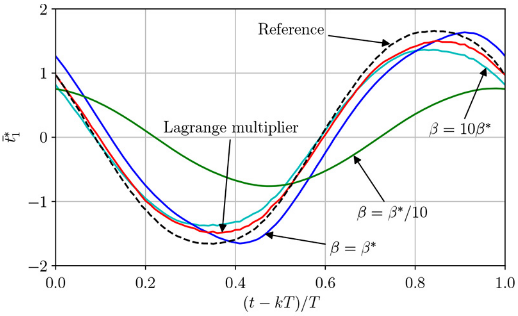

Figure 10.
The component, $\bar{t}_1^*$, of the resultant non-dimensionalised traction, exerted on the cylinder in the x_1-direction by the fluid and calculated by the Lagrange multiplier and penalty methods using the intermediate mesh and a time step of $\Delta t = T/100$, plotted as a function of non-dimensionalised time $(t - kT)/T$, where k is a whole number and $k \geq 4$

Notes: Also shown is $\tilde{t}_1^*$ from the solution of Dütsch *et al.* (1998), which was obtained using a defined-body method and is used here as a reference. The quantity T is the period of motion of the cylinder. The values from the penalty method are shown for three penalty factors: $\beta = \beta^*/10$, β^* and $10\beta^*$, where β^* is the recommended penalty factor
(a) Lagrange multiplier approach; (b) Penalty approach

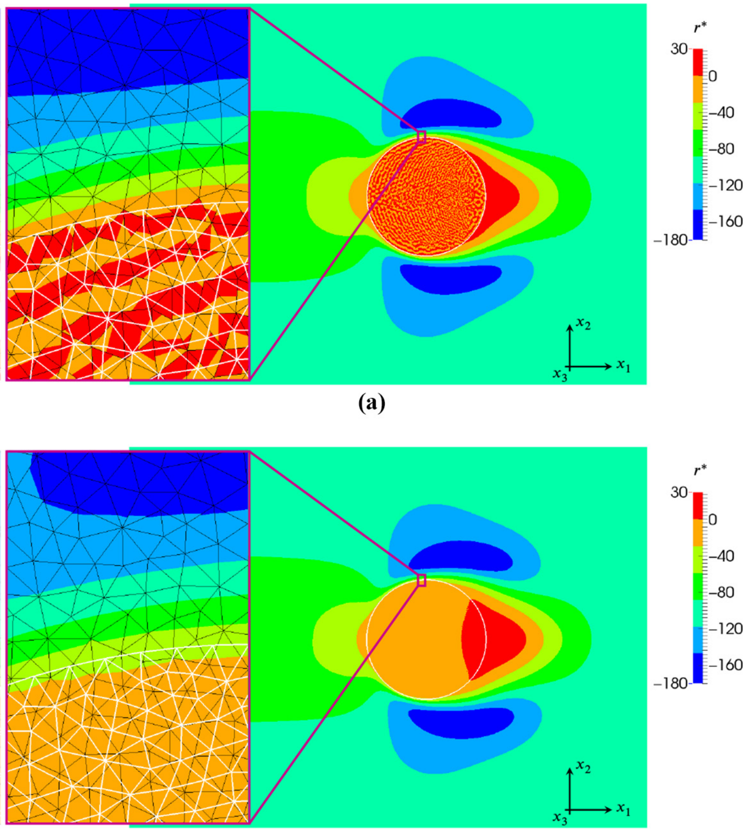

(a)

(b)

Figure 11. Contours of the normalised component, $r^*(\mathrm{x},t)$, that acts in the x_1-direction, of the velocity of the fluid relative to that of the cylinder is shown in (a) for the Lagrange multiplier approach and in (b) for the penalty approach with $\beta = \beta^*$

Notes: The contours shown are at a time of $t = kT$, with T being the period of motion of the cylinder and k being a whole number, $k \geq 4$. The white circle represents the wetted boundary $\partial\Omega_s$ of the cylinder and the white elements are from the solid mesh Ω_s^h

observed for the Lagrange multiplier method, but are still considered small enough for the solutions for $\beta = 10\beta^*$ to be deemed converged with respect to mesh spacing. In contrast, the curves for $\beta = \beta^*/10$ and $\beta = \beta^*$ remaining almost constant when moving from the coarse mesh to the intermediate mesh, and the drop sharply when moving on to the fine mesh. In Figure 12(b), as expected r_t^* from the penalty method for $\beta = \beta^*/10$ and $\beta = \beta^*$ decrease monotonically as Δt is reduced. However, in both of these cases this decrease is at least 10% between consecutive time steps and shows that the solutions obtained are not time step independent. The curve for $\beta = 10\beta^*$ actually increases slightly, by less than 5% when comparing the value of r_t^* at $\Delta t = T/50$ to that at $\Delta t = T/250$, as Δt is reduced. The rate of increase of the curve is relatively small and it may be caused by the surrogate boundary under – or overcompensating for the smearing of $\partial\Omega_s$. The solutions for $\beta = 10\beta^*$ are, therefore, considered to be converged with respect to time step refinement.

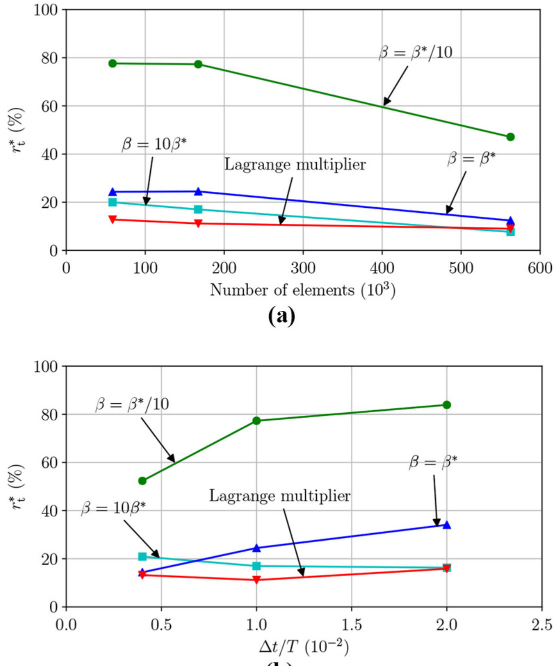

(a)

(b)

Notes: The reference solution is from Dütsch *et al.* (1998) and was calculated using a defined-body method. The quantity r_t^* is plotted in (a) as a function of the number of elements in the computational mesh of the overall domain and in (b) as a function of the non-dimensionalised time step $\Delta t/T$, where T is the period of motion of the cylinder. The data is taken from the portion of the time domain after the flow field has become periodic ($t \geq 4T$). The data from the penalty method is plotted for three penalty factors $\beta = \beta^*/10$, β^* and $10\beta^*$, where β^* is the recommended penalty factor

Figure 12.
Shown is the non-dimensionalised root mean square, r_t^*, of the difference between the x_1-component of the traction, exerted on the cylinder by the fluid, from the Lagrange multiplier and penalty methods and the value of this component from the reference solution

Similarly, the curve for the Lagrange multiplier method decreases by 2% from $\Delta_t = T/50$ to $\Delta t = T/100$, but then increases by 5% from $\Delta t = T/100$ to $\Delta t = T/250$. Once again, as this increase is small, it may be caused by the surrogate boundary. The solutions from the Lagrange multiplier method are, therefore also deemed to be converged with respect to time step refinement. Furthermore, as was the case for the error in the velocity field of the channel flow test problem, the value of r_t^* diminishes as β is raised in both Figures 12(a) and 12(b), except when the intermediate mesh is used together with $\Delta t = T/250$.

Computational times are plotted in Figure 13(a) as a function of the number of mesh elements for $\Delta t/T = 1/100$. They are also plotted in Figure 13(b) as a function of $\Delta t/T$ for the intermediate mesh. The computational times are calculated in the manner described in

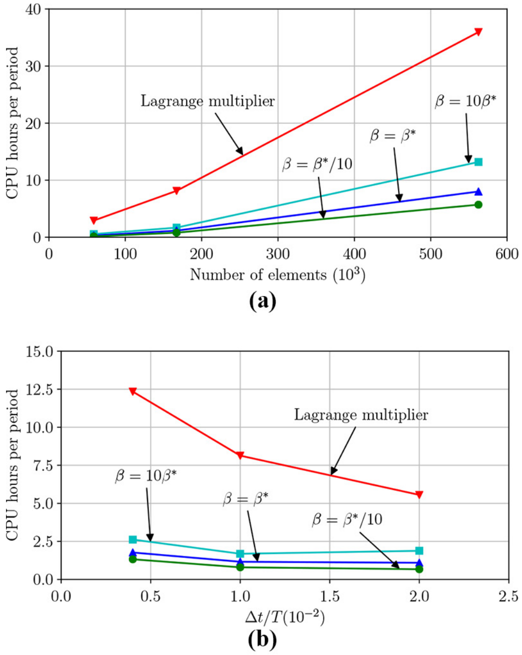

Figure 13. Computational times for the Lagrange multiplier method and the penalty method for penalty factors $\beta = \beta^*/10, \beta^*$ and $10\beta^*$, where β^* is the recommended penalty factor

Notes: Each computational time shown is the total CPU hours needed by the solver to calculate the flow field for one period of motion T of the cylinder The data is taken from the portion of the time domain after the flow field has become periodic ($t \geq 4T$) and is plotted in (a) as a function of the number of elements in the computational mesh of the overall domain and in (b) as a function of non-dimensionalised time step $\Delta t/T$.

Section 5.1 for one period of motion of the cylinder after the flow field has reached steady-state. Both figures show that the computational times needed by the Lagrange multiplier method are again larger than those required by the penalty method. Also, the computational times of the penalty method again escalate as the value of β is increased. As before, this is because of an increase in the number of solver and non-linear iterations required to reach convergence. Although this test problem does not have an analytical solution, the conclusions based on the reference numerical solution indicate a similar pattern as for the channel flow test problem, namely, that the Lagrange multiplier method provides a robust and accurate method that does not require calibration. These advantages come at the cost of increased computation time compared to the penalty method.

5.3 Vortex-induced vibration of a cylinder

The final test problem examines the vortex-induced vibration of a cylinder in the presence of an oncoming flow. The vibration of the cylinder is expected to be similar to the motion observed in the harmonic motion test problem in Section 5.2. The computational domain used is, therefore, identical to that from the harmonic motion problem and is illustrated in Figure 8. The "intermediate mesh", described in Section 5.2 and shown in Figure 9, is also selected as the computational mesh as both the Lagrange multiplier and penalty methods were able to produce solutions that were sufficiently converged in terms of mesh refinement. Correspondingly, a time step of $\Delta t = T/100$ was chosen, where T is the prescribed period of motion of the cylinder in Section 5.2, as both methods were able to provide sufficiently converged solutions with respect to time step refinement. The boundary conditions at the sides of the domain are kept the same. At the top and bottom boundaries, the boundary conditions are replaced with $\mathbf{u} = u_\infty \mathbf{e}_2$ and $\boldsymbol{\sigma}\mathbf{n} = \mathbf{0}$, respectively. The value of the inlet speed u_∞ is selected to obtain a Reynolds number of $Re_D = \rho u_\infty D/\mu = 150$, with D being the diameter of the cylinder.

The response of the cylinder is governed by equation (8), with m (its mass) being selected to provide a mass ratio of $m^* = 4m/\rho\pi D^2 = 2$. The values of k and c are set such that the appropriate damping ratio $\zeta = c/2\sqrt{mk}$ and reduced velocity $u_\mathrm{r}^* = DT_\mathrm{n}u_\infty$ are obtained, where $T_\mathrm{n} = 2\pi\sqrt{m/k}$ and is the undamped natural period of motion of the single-degree-of-freedom system. The penalty and Lagrange multiplier methods are each used to simulate the scenarios $u_\mathrm{r}^* = 6$ (resonance) and $u_\mathrm{r}^* = 10$. In each scenario, the penalty method simulations are conducted for three different penalty factors: $\beta = \beta^*/10$, β^* and $10\beta^*$.

The motion of the cylinder in the x_1-direction is depicted in Figure 14 as a function of t/T_d for $u_\mathrm{r}^* = 6$, where $T_\mathrm{d} = T_\mathrm{n}/\sqrt{1-\zeta^2}$ and is the damped natural period of the system. For each simulation, the cylinder was first held stationary for 2,000 time steps. The cylinder is then released at $t/T_\mathrm{d} = 0$ and allowed to vibrate under the influence of the fluid. Also plotted is the amplitude of motion from the solution of Carmo *et al.* (2011), which was calculated using a DB method and is used here as a reference. Despite $\beta = 10\beta^*$ generally yielding the most accurate calculations of the traction from the penalty method in Section 5.2, this penalty factor now causes the method to diverge before the cylinder completes a single

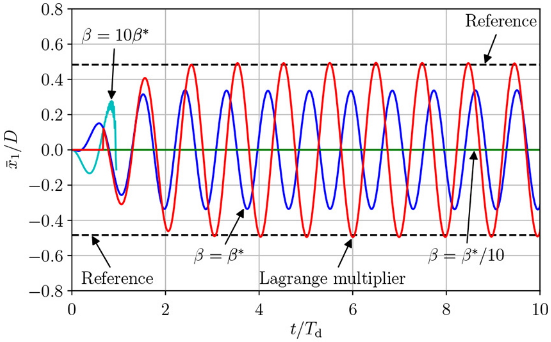

Notes: Also shown is the amplitude of motion from the solution of Carmo *et al.* (2011), which was calculated using a defined-body method and is used here as a reference. The quantity T_d is the damped natural period of the structural model. The motions from the penalty method are shown for three penalty factors: $\beta = \beta^*/10$, β^* and $10\beta^*$, where β^* is the recommended penalty factor

Figure 14.
The x_1-coordinate, $\bar{x}_1$, of the centre of gravity of the cylinder, non-dimensionalised using the cylinder diameter D and calculated using the penalty and Lagrange multiplier methods, plotted as a function of non-dimensionalised time, t/T_d

oscillation. This again demonstrates a major drawback of the penalty method, which is that the optimal penalty factor is difficult to determine a priori, and is highly problem dependent. The Lagrange multiplier method calculates an amplitude that is only slightly larger than that from the reference solution. During the interval $0 \leq t/T_\mathrm{d} \leq 2$, the penalty method with $\beta = \beta^*$ predicts a transient behaviour that is roughly similar to that from the Lagrange multiplier method. However, once the cylinder settles into its steady-state motion, it is apparent that it exhibits a much lower amplitude, as well as a different period and phase. When $\beta = \beta^*/10$, the no-slip condition is not enforced strongly enough to create the vorticity required to excite the cylinder.

The differences observed for $u_\mathrm{r}^* = 6$ between the vibration of the cylinder predicted for $\beta = \beta^*$ and that from the Lagrange multiplier method are clarified by the snapshots in Figure 15. The snapshots show streamlines of the non-dimensionalised fluid velocity $\mathbf{u}^* = DT_\mathrm{n}\mathbf{u}$ at two moments, namely, $t/T_\mathrm{d} = 9.475$ and $t/T_\mathrm{d} = 9.725$. At each of these moments, the location of the cylinder is roughly the same in both solutions. In each snapshot, the colours

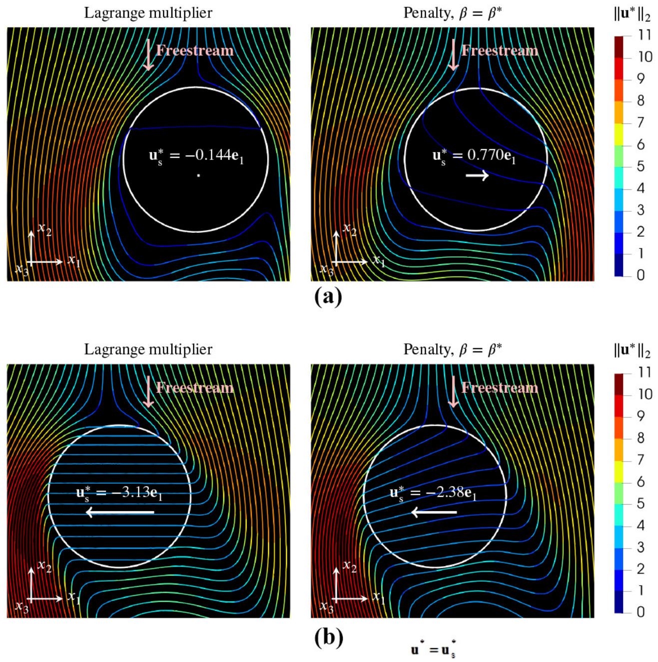

Notes: The streamlines are depicted in (a) at $t/T_\mathrm{d} = 9.475$ and in (b) at $t/T_\mathrm{d} = 9.725$ for both the Lagrange multiplier method and the penalty method with $\beta = \beta^*$, where T_d is the damped natural period of motion of the cylinder and β^* is the recommended penalty factor. The white circle represents the wetted boundary $\partial\Omega_\mathrm{s}$ of the cylinder and the white arrow is the direction it is moving in. The quantity $\mathbf{u}_\mathrm{s}^*$ is the non-dimensionalised velocity field of the cylinder, which is constant as it is experiencing pure translation. If the no-slip condition is being imposed correctly, the streamlines should be horizontal and $\mathbf{u}^* = \mathbf{u}_\mathrm{s}^*$ inside of $\partial\Omega_\mathrm{s}$

Figure 15.
Shown are streamlines of the non-dimensionalised fluid velocity $\mathbf{u}^*$

of the streamlines reflect the values of $\|\mathbf{u}^*\|_2$ and the white circle represents $\partial\Omega_\mathrm{s}$. Also shown is the direction of the free stream flow, which approaches the cylinder from the top, and the non-dimensionalised cylinder velocity $\mathbf{u}_\mathrm{s}^* = DT_\mathrm{n}\mathbf{u}_\mathrm{s}$. For the no-slip condition to be imposed correctly, it is required that $\mathbf{u}^* = \mathbf{u}_\mathrm{s}^*$ inside of Ω_s. Furthermore, as the cylinder is experiencing pure translation in the x_1-direction, the streamlines should be horizontal in this region. The Lagrange multiplier method comes very close to meeting these requirements at both $t/T_\mathrm{d} = 9.475$ and $t/T_\mathrm{d} = 9.725$. In contrast, the streamlines for $\beta = \beta^*$ are not horizontal, and the magnitude of $\mathbf{u}^*$ varies greatly inside of Ω_s. A large amount of the oncoming flow is, therefore, passing through this region, instead of being directed around it as theoretically required by the penalty method.

The steady-state amplitude A and actual period of motion T of the cylinder, non-dimensionalised with respect to D and T_d, respectively, are presented in Table 1 for $u_\mathrm{r}^* = 6$ and $u_\mathrm{r}^* = 10$. Also shown are the corresponding values of A/D and T/T_d from the reference solution (Carmo *et al.*, 2011). The results for $\beta = \beta^*/10$ are omitted as in both scenarios the cylinder exhibits no oscillations in the steady-state solution. As already seen in Figure 14, A/D from the Lagrange multiplier method is closest to that from the reference solution for $u_\mathrm{r}^* = 6$, with a difference of 3%. However, it is also nearest to the A/D of the reference solution for $u_\mathrm{r}^* = 10$, with the difference being 5%. For $u_\mathrm{r}^* = 6$, the penalty method diverges with $\beta = 10\beta^*$ and with $\beta = \beta^*$ it underpredicts the reference A/D by 30%. The penalty method does converge with $\beta = 10\beta^*$ for $u_\mathrm{r}^* = 10$, and gets much closer to the reference A/D than with $\beta = \beta^*$, but still overpredicts it by 13%. The value of T/T_d from the Lagrange multiplier method also shows the best agreement with that of the reference solution for both $u_\mathrm{r}^* = 6$ and $u_\mathrm{r}^* = 10$, being 2% lower and 18% higher, respectively. Despite having difficulty in predicting the A/D for $u_\mathrm{r}^* = 6$, the penalty method with $\beta = \beta^*$ actually yields a value for T/T_d that is quite similar to that of the reference for this case, as it comes within 12% of it. However, as with the Lagrange multiplier method, the penalty method significantly overpredicts T/T_d by 19% for $u_\mathrm{r}^* = 10$, both with $\beta = \beta^*$ and $\beta = 10\beta^*$. As in the previous two test problems, the Lagrange multiplier method delivered an accurate solution without the need to calibrate parameters. In contrast to the two previous problems, a larger value of the penalty factor did not improve the solution. The best value from the penalty method was obtained using the recommended penalty factor, but the accuracy of the solution was in general still lower than that from the Lagrange multiplier method.

Table 1. Amplitude A and period T of the motion of the cylinder, non-dimensionalised with respect to its diameter D and its natural period of motion T_d, respectively, as calculated by the Lagrange multiplier and penalty methods

Case	Method	A/D	T/T_d
$u_\mathrm{r}^* = 6$	Reference	0.478	1.00
	$\beta = \beta^*$	0.337	0.887
	$\beta = 10\beta^*$	Diverged	
	DLM	0.492	0.984
$u_\mathrm{r}^* = 10$	Reference	0.0790	0.599
	$\beta = \beta^*$	0.118	0.709
	$\beta = 10\beta^*$	0.0920	0.709
	DLM	0.0752	0.704

Notes: The values are presented for the case $u_\mathrm{r}^* = 6$ (resonance) and $u_\mathrm{r}^* = 10$, where u_r^* is the reduced velocity. Also shown as reference are the values from the solution of Carmo *et al.* (2011), which were calculated using a defined-body method. The values from the penalty method are provided for two penalty factors: $\beta = \beta^*$ and $10\beta^*$, where β^* is the recommended penalty factor. For $u_\mathrm{r}^* = 6$, the penalty method diverges when $\beta = 10\beta^*$

6. Conclusions

A detailed comparative analysis has been conducted to evaluate the performance of the penalty and Lagrange multiplier approaches. For each approach, the analysis investigated the accuracy with which the no-slip condition is enforced and the effect this has on the overall solution, as well as the associated computational cost. Three different test problems were considered, namely, laminar flow through a channel, the harmonic motion of a cylinder through a stationary fluid and the vortex-induced vibration of a cylinder.

The findings indicated that the Lagrange multiplier approach is able to enforce the no-slip condition much more accurately than the penalty approach. Correspondingly, the Lagrange multiplier approach provided better predictions of both the steady-state flow field in the channel flow problem, and the response of the cylinder in the vortex-induced vibration problem. In the channel flow problem, both the Lagrange multiplier method and penalty method exhibited linear convergence of the velocity and pressure fields with respect to mesh refinement. However, when it came to the error in enforcing the no-slip condition, the convergence rate of the penalty method dropped far below linear. In the harmonic motion problem, the Lagrange multiplier and penalty methods were both able to predict the resultant tractions with similar levels of accuracy. Therefore, imposing the no-slip condition with less error resulted in the Lagrange multiplier method providing solutions that were of either equivalent or superior accuracy relative to those from the penalty method. For each test problem in which it was measured, the Lagrange multiplier method also required more computational time than the penalty method to arrive at a solution.

For the penalty approach, the error incurred in the imposition of the no-slip condition and in the overall solution, and the computational time needed were observed to be dependent on the value of the penalty factor. In the channel flow and harmonic motion test problems, both the accuracy of the enforcement of the no-slip condition and the overall solution improved in general as the penalty factor was increased. However, as shown by the vortex-induced vibration problem, the penalty approach will actually diverge if the penalty factor is pushed too high. The appropriate value to assign to the penalty factor is, therefore, difficult to determine a priori as it depends on the problem being considered, as well as the computational mesh and time step. Furthermore, the computational time needed by the penalty approach increased as the penalty factor was increased. Thus, when the penalty factor was raised to improve the accuracy of the solution to a similar level as that provided by the Lagrange multiplier approach in the channel flow test problem, the computational times of the two approaches also became roughly similar, although those from the penalty approach were still the shortest.

In summary, this study shows that the primary advantages of the Lagrange multiplier approach were that it provides an accurate solution, especially when enforcing the no-slip condition, while being robust as it does not require the "tuning" of any problem specific parameters. However, these benefits came at a relatively high computational cost when compared to the penalty approach. In contrast, the penalty approach featured a simpler formulation and shorter computational times, but it required that the appropriate value be assigned to the penalty factor for it to yield accurate results. Furthermore, the appropriate value of the penalty factor was difficult to determine ahead of time, and if too large of a value was selected the penalty approach diverged. It is noteworthy to point out that the bodies considered in this study were thick or bluff. Both the Lagrange multiplier and penalty approaches of the immersed boundary method have also already been applied to thin bodies in the literature such as in Taira and Colonius (2007), Viré *et al.* (2015) and Kadapa *et al.* (2016). However, it would be useful to carry out a similar comparative analysis of these approaches for thin bodes.

References

Amicarelli, A., Kocak, B., Sibilla, S. and Grabe, J. (2017), “A 3D smoothed particle hydrodynamics model for erosional dam-break floods”, *International Journal of Computational Fluid Dynamics*, Vol. 31 No. 10, pp. 413-434, doi: 10.1080/10618562.2017.1422731.

Bazilevs, Y., Hsu, M.-C., Kiendl, J., Wüchner, R. and Bletzinger, K.-U. (2011), “3D simulation of wind turbine rotors at full scale. Part II: fluid-structure interaction modeling with composite blades”, *International Journal for Numerical Methods in Fluids*, Vol. 65 No. 1-3, pp. 236-253, doi: 10.1002/fld.2454.

Boffi, D. and Gastaldi, L. (2017), “A fictitious domain approach with Lagrange multiplier for fluid-structure interactions”, *Numerische Mathematik*, Vol. 135 No. 3, pp. 711-732, doi: 10.1007/s00211-016-0814-1.

Boffi, D., Cavallini, N. and Gastaldi, L. (2015), “The finite element immersed boundary method with distributed Lagrange multiplier”, *SIAM Journal on Numerical Analysis*, Vol. 53 No. 6, pp. 2584-2604, doi: 10.1137/140978399.

Brandsen, J.D., Van der Spuy, S.J. and Venter, G. (2018), “Prediction of axial compressor blade excitation by using a two-way staggered fluid-structure interaction model”, *Proceedings of the Institution of Mechanical Engineers, Part G: Journal of Aerospace Engineering*, Vol. 232 No. 8, pp. 1495-1514, doi: 10.1177/0954410017694056.

Carmo, B.S., Sherwin, S.J., Bearman, P.W. and Willden, R.H.J. (2011), “Flow-induced vibration of a circular cylinder subjected to wake interference at low Reynolds number”, *Journal of Fluids and Structures*, Vol. 27 No. 4, pp. 503-522, doi: 10.1016/j.jfluidstructs.2011.04.003.

Cotter, C.J., Ham, D.A. and Pain, C.C. (2009), “A mixed discontinuous/continuous finite element pair for shallow-water ocean modelling”, *Ocean Modelling*, Vol. 26 Nos 1/2, pp. 86-90, doi: 10.1016/j.ocemod.2008.09.002.

Dütsch, H., Durst, F., Becker, S. and Lienhart, H. (1998), “Low-Reynolds-number flow around an oscillating circular cylinder at low Keulegan-Carpenter numbers”, *Journal of Fluid Mechanics*, Vol. 360, pp. 249-271, doi: 10.1017/S002211209800860X.

Farrell, P.E. and Maddison, J.R. (2011), “Conservative interpolation between volume meshes by local Galerkin projection”, *Computer Methods in Applied Mechanics and Engineering*, Vol. 200 No. 1-4, pp. 89-100, doi: 10.1016/j.cma.2010.07.015.

Farrell, P.E., Piggott, M.D., Pain, C.C., Gorman, G.J. and Wilson, C.R. (2009), “Conservative interpolation between unstructured meshes via supermesh construction”, *Computer Methods in Applied Mechanics and Engineering*, Vol. 198 No. 33-36, pp. 2632-2642, doi: 10.1016/j.cma.2009.03.004.

Gao, X., Zhang, Q. and Tang, Q. (2016), “Numerical modelling of mars supersonic disk-gap-band parachute inflation”, *Advances in Space Research*, Vol. 57 No. 11, pp. 2259-2272, doi: 10.1016/j.asr.2016.03.010.

Glowinski, R., Pan, T.W. and Périaux, J. (1998), “Distributed Lagrange multiplier methods for incompressible viscous flow around moving rigid bodies”, *Computer Methods in Applied Mechanics and Engineering*, Vol. 151 No. 1-2, pp. 181-194, doi: 10.1016/S0045-7825(97)00116-3.

Glowinski, R., Pan, T.-W. and Périaux, J. (1997), “A Lagrange multiplier/fictitious domain method for the numerical simulation of incompressible viscous flow around moving rigid bodies: (I) case where the rigid body motions are known a priori”, *Comptes Rendus de L'académie Des Sciences – Series I – Mathematics*, Vol. 324 No. 3, pp. 361-369, doi: 10.1016/S0764-4442(99)80376-0.

Glowinski, R., Pan, T.-W., Kearsley, A.J. and Périaux, J. (1995), “Numerical simulation and optimal shape for viscous flow by a fictitious domain method”, *International Journal for Numerical Methods in Fluids*, Vol. 20 No. 8-9, pp. 695-711, doi: 10.1002/fld.1650200803.

Goldstein, D., Handler, R. and Sirovich, L. (1993), “Modeling a no-slip flow boundary with an external force field”, *Journal of Computational Physics*, Vol. 105 No. 2, pp. 354-366, doi: 10.1006/jcph.1993.1081.

Gong, S.W. (2019), "Transient response of stiffened composite submersible hull to underwater shock and bubble", *Composite Structures*, Vol. 213, pp. 243-251, doi: 10.1016/j.compstruct.2019.01.097.

Kadapa, C., Dettmer, W.G. and Perić, D. (2016), "A fictitious domain/distributed Lagrange multiplier based fluid-structure interaction scheme with hierarchical B-spline grids", *Computer Methods in Applied Mechanics and Engineering*, Vol. 301, pp. 1-27, doi: 10.1016/j.cma.2015.12.023.

Khadra, K., Angot, P., Parneix, S. and Caltagirone, J.-P. (2000), "Fictitious domain approach for numerical modelling of Navier-Stokes equations", *International Journal for Numerical Methods in Fluids*, Vol. 34 No. 8, pp. 651-684, doi: 10.1002/1097-0363(20001230)34:8¡651::AID-FLD61¿3.0.CO;2-D.

Kim, Y. and Peskin, C.S. (2016), "A penalty immersed boundary method for a rigid body in fluid", *Physics of Fluids*, Vol. 28 No. 3, p. 033603, doi: 10.1063/1.4944565.

Lācis, U., Taira, K. and Bagheri, S. (2016), "A stable fluid-structure-interaction solver for low-density rigid bodies using the immersed boundary projection method", *Journal of Computational Physics*, Vol. 305, pp. 300-318, doi: 10.1016/j.jcp.2015.10.041.

Mittal, R. and Iaccarino, G. (2005), "Immersed boundary methods", *Annual Review of Fluid Mechanics*, Vol. 37 No. 1, pp. 239-261, doi: 10.1146/annurev.fluid.37.061903.175743.

Pain, C.C., Umpleby, A.P., De Oliveira, C.R.E. and Goddard, A.J.H. (2001), "Tetrahedral mesh optimisation and adaptivity for steady-state and transient finite element calculations", *Computer Methods in Applied Mechanics and Engineering*, Vol. 190 No. 29-30, pp. 3771-3796, doi: 10.1016/S0045-7825(00)00294-2.

Pain, C.C., Piggott, M.D., Goddard, A.J.H., Fang, F., Gorman, G.J., Marshall, D.P. and de Oliveira, C.R.E. (2005), "Three-dimensional unstructured mesh ocean modelling", *Ocean Modelling*, Vol. 10 Nos 1/2, pp. 5-33, doi: 10.1016/j.ocemod.2004.07.005.

Peskin, C.S. (1972), "Flow patterns around heart valves: a numerical method", *Journal of Computational Physics*, Vol. 10 No. 2, pp. 252-271, doi: 10.1016/0021-9991(72)90065-4.

Piggott, M.D., Gorman, G.J., Pain, C.C., Allison, P.A., Candy, A.S., Martin, B.T. and Wells, M.R. (2008), "A new computational framework for multi-scale ocean modelling based on adapting unstructured meshes", *International Journal for Numerical Methods in Fluids*, Vol. 56 No. 8, pp. 1003-1015, doi: 10.1002/fld.1663.

Sodja, J., De Breuker, R., Nozak, D., Drazumeric, R. and Marzocca, P. (2018), "Assessment of low-fidelity fluid-structure interaction model for flexible propeller blades", *Aerospace Science and Technology*, Vol. 78, pp. 71-88, doi: 10.1016/j.ast.2018.03.044.

Specklin, M. and Delauré, Y. (2018), "A sharp immersed boundary method based on penalization and its application to moving boundaries and turbulent rotating flows", *European Journal of Mechanics – B/Fluids*, Vol. 70, pp. 130-147, doi: 10.1016/j.euromechflu.2018.03.003.

Sun, P. (2019), "Fictitious domain finite element method for stokes/elliptic interface problems with jump coefficients", *Journal of Computational and Applied Mathematics*, Vol. 356, pp. 81-97, doi: 10.1016/j.cam.2019.01.030.

Taira, K. and Colonius, T. (2007), "The immersed boundary method: a projection approach", *Journal of Computational Physics*, Vol. 225 No. 2, pp. 2118-2137, doi: 10.1016/j.jcp.2007.03.005.

Verma, S., Abbati, G., Novati, G. and Koumoutsakos, P. (2017), "Computing the force distribution on the surface of complex, deforming geometries using vortex methods and brinkman penalization", *International Journal for Numerical Methods in Fluids*, Vol. 85 No. 8, pp. 484-501, doi: 10.1002/fld.4392.

Viré, A., Xiang, J. and Pain, C.C. (2015), "An immersed-shell method for modelling fluid-structure interactions", *Philosophical Transactions of the Royal Society A: Mathematical, Physical and Engineering Sciences*, Vol. 373 No. 2035, doi: 10.1098/rsta.2014.0085.

Viré, A., Spinneken, J., Piggott, M.D., Pain, C.C. and Kramer, S.C. (2016), "Application of the immersed-body method to simulate wave-structure interactions", *European Journal of Mechanics – B/Fluids*, Vol. 55, pp. 330-339, doi: 10.1016/j.euromechflu.2015.10.001.

Viré, A., Xiang, J., Milthaler, F., Farrell, P.E., Piggott, M.D., Latham, J.-P., Pavlidis, D. and Pain, C.C. (2012), "Modelling of fluid-solid interactions using an adaptive mesh fluid model coupled with a combined finite-discrete element model", *Ocean Dynamics*, Vol. 62 Nos 10/12, pp. 1487-1501, doi: 10.1007/s10236-012-0575-z.

Yan, J., Korobenko, A., Deng, X. and Bazilevs, Y. (2016), "Computational free-surface fluid-structure interaction with application to floating offshore wind turbines", *Computers and Fluids*, Vol. 141, pp. 155-174, doi: 10.1016/j.compfluid.2016.03.008.

Corresponding author
Jacobus Brandsen can be contacted at: j.d.brandsen@tudelft.nl